

## University of Dayton eCommons

---

Electrical and Computer Engineering Faculty  
Publications

Department of Electrical and Computer  
Engineering

---

9-2009

# Anomaly Detection in Hyperspectral Imagery: Comparison of Methods Using Diurnal and Seasonal Data


Patrick C. Hytla  
*University of Dayton*

Russell C. Hardie  
*University of Dayton, [rhardie1@udayton.edu](mailto:rhardie1@udayton.edu)*

Michael T. Eismann  
*Air Force Research Laboratory*

Joseph Meola  
*Air Force Research Laboratory*

Follow this and additional works at: [https://ecommons.udayton.edu/ece\\_fac\\_pub](https://ecommons.udayton.edu/ece_fac_pub)

 Part of the [Optics Commons](#), [Other Engineering Commons](#), and the [Signal Processing Commons](#)

---

### eCommons Citation

Hytla, Patrick C.; Hardie, Russell C.; Eismann, Michael T.; and Meola, Joseph, "Anomaly Detection in Hyperspectral Imagery: Comparison of Methods Using Diurnal and Seasonal Data" (2009). *Electrical and Computer Engineering Faculty Publications*. 10. [https://ecommons.udayton.edu/ece\\_fac\\_pub/10](https://ecommons.udayton.edu/ece_fac_pub/10)

This Article is brought to you for free and open access by the Department of Electrical and Computer Engineering at eCommons. It has been accepted for inclusion in Electrical and Computer Engineering Faculty Publications by an authorized administrator of eCommons. For more information, please contact [frice1@udayton.edu](mailto:frice1@udayton.edu), [mschlangen1@udayton.edu](mailto:mschlangen1@udayton.edu).

# Anomaly detection in hyperspectral imagery: comparison of methods using diurnal and seasonal data

Patrick C. Hytla,<sup>a</sup> Russell C. Hardie,<sup>a</sup> Michael T. Eismann,<sup>b</sup>  
and Joseph Meola<sup>b</sup>

<sup>a</sup>University of Dayton, 300 College Park Drive, Dayton OH 45469

<sup>b</sup>Air Force Research Laboratory, 2241 Avionics Circle,  
Wright-Patterson AFB, OH 45433

**Abstract.** The use of hyperspectral imaging is a fast growing field with many applications in the civilian, commercial and military sectors. Hyperspectral images are typically composed of many spectral bands in the visible and infrared regions of the electromagnetic spectrum and have the potential to deliver a great deal of information about a remotely sensed scene. One area of interest regarding hyperspectral images is anomaly detection, or the ability to find spectral outliers within a complex background in a scene with no *a priori* information about the scene or its specific contents. Anomaly detectors typically operate by creating a statistical background model of a hyperspectral image and measuring anomalies as image pixels that do not conform properly to that given model. In this study we compare the performance over diurnal and seasonal changes for several different anomaly detection methods found in the literature and a new anomaly detector that we refer to as the fuzzy cluster-based anomaly detector. Here we also compare the performance of several anomaly-based change detection algorithms. Our results indicate that all anomaly detectors tested in this experimentation exhibit strong performance under optimum illumination and environmental conditions. However, our results point toward a significant performance advantage for cluster-based anomaly detectors in the presence of adverse environmental conditions.

**Keywords:** anomaly detection; hyperspectral imagery; change detection.

## 1 INTRODUCTION

Hyperspectral imaging (HSI) is a field of growing interest with civilian, commercial and military applications. Applications of HSI include surveillance, search and rescue operations, geological feature classification, and military target and threat detection [1-6]. Unlike conventional imaging systems that gather broadband radiance from the scene, hyperspectral imaging employs an imaging spectrometer to detect and extract information in many spectral bands. The spectral information generally includes the visible and infrared regions of the electromagnetic spectrum.

The wealth of data captured from hyperspectral remote sensing instruments allows for in-depth spectral analysis of images not possible with conventional panchromatic or even multispectral images. However, in most real world applications, the analysis of the collected data is hampered because little information about the target scene is known prior to processing. One image processing technique capable of exploiting spectral information without *a priori* knowledge of the scene is anomaly detection. One variant of this technique creates a statistical background model for an image and detects spectral outliers (anomalies) that do not fit that background model. Many methods have been developed to calculate the background model's probability density function (pdf) in order to reduce false alarms and

improve overall anomaly detection performance. These are covered thoroughly in existing literature [5,7,8]. In this study, several different types of anomaly detection methods are applied to a test scene with diurnal and seasonal changes in order to measure overall detection performance. In addition to comparing several detectors found in existing literature, a novel method referred to here as fuzzy cluster-based anomaly detection (FCBAD) is introduced. We believe this method may offer more flexibility and versatility than existing methods. Anomaly detectors can also be used to detect anomalous change between two images of the same scene captured some time interval apart. The main components in the change detection process are a predictor and an anomaly detector. In this study we investigate the performance of several prediction-anomaly detection combinations.

The remainder of this paper is organized as follows: The anomaly detectors are described in detail in Section 2. Change detection is discussed in Section 3. Section 4 explains the test scene setup, the data collection process and the calibration procedures utilized to generate accurate hyperspectral images for analysis. The results and conclusions drawn from the study are described in Sections 5 and 6, respectively.

## 2 ANOMALY DETECTION ALGORITHMS

This section defines the anomaly detection algorithms compared in this study. To begin, a hyperpixel is defined as a vector corresponding to all the spectral measurements for a single pixel and is denoted here as

$$\mathbf{z} = [z_1, z_2, \dots, z_N]^T, \quad (1)$$

where  $N$  is the number of hyperspectral bands present in the image. Anomaly detectors are generally based on a distance metric to a known background class, some of which are derived from a likelihood ratio test (LRT) [6] given by

$$L(\mathbf{z}) = \frac{p_1(\mathbf{z})}{p_0(\mathbf{z})} > T, \quad (2)$$

where  $p_0(\mathbf{z})$  is the hyperpixel probability density function (pdf) under the assumption that only background and no target is present. The pdf  $p_1(\mathbf{z})$  is the pdf for the where a target is present, and  $T$  is some detection threshold. The discriminant function, or decision statistic, for the LRT is given by

$$d(\mathbf{z}) = \log(p_1(\mathbf{z})) - \log(p_0(\mathbf{z})). \quad (3)$$

Many anomaly detectors can be cast into this framework by setting the pdf  $p_1(\mathbf{z})$  to be a constant to reflect a lack of knowledge about a target class (making it a uniform pdf). Under these conditions, the decision statistic in (3) effectively simplifies to

$$d(\mathbf{z}) = -\log(p_0(\mathbf{z})). \quad (4)$$

The background models generally used in (4) can be categorized into three basic types: global, locally adaptive, and cluster-based. Global models use one pdf across the entire image. A Gaussian pdf is a common choice for such methods. An extension of this simple global model assumes the background consists of a superposition of several Gaussians. Locally adaptive methods calculate scene statistics utilizing a sliding window. Cluster-based

models attempt to break the image pixels into clusters, or classes, based on similarities between pixels and compute background statistics for each cluster.

In this experimentation, targets are man-made objects while the background consists of all other non man-made objects. Statistics used in background modeling are computed directly from experimental data. For part of the study, the known targets are excluded from the statistical calculations and modeling of the background. This represents the ideal case of background modeling. In more realistic scenarios, however, targets will be present and thus incorporated into the background statistics. In order to test algorithm performance under more realistic circumstances, target pixels are allowed to contaminate the background model in a separate part of the study.

The background statistics for the cluster-based methods are computed from either a k-means clustering algorithm [9] or a stochastic expectation maximization algorithm (SEM) [10,11]. The k-means algorithm is an iterative process that is initialized by picking evenly spaced vectors of image hyperpixels to create initial class statistics. Each hyperpixel is then assigned to a class based on a linear Euclidean distance classification. After the first assignment, the statistics are recomputed and new class assignments are made. This process is repeated until convergence. The SEM algorithm is also an iterative process. In this study, the classes are initialized using the global sample statistics for all classes. After initialization, each hyperpixel is assigned to a class through the use of a stochastic quadratic classifier. New class statistics are then computed based on the new class assignments and the process continues in an iterative fashion until convergence.

The goal of each anomaly detector is to identify the man-made objects in a natural background under varying seasonal and diurnal conditions. Each anomaly detector employed in this study is listed in Table 1 and further explained in this section.

Table 1: Anomaly Detector Identification.

Algorithm Name	Acronym	Features
Mahalanobis Distance	M-dist	single background class for entire image
Gaussian Mixture Model	GMM	superposition of $K$ -Gaussians, soft class boundaries, SEM clustering
Reed-Xiaoli	RX	locally adaptive method
Gaussian Mixture RX	GMRX	similar to GMM, requires posteriori probability, SEM clustering
Cluster-Based Anomaly Detection	CBAD	does not assume Gaussian, hard class boundaries, k-means clustering
Fuzzy Cluster Based Anomaly Detection	FCBAD	does not assume Gaussian, can use several membership functions, k-means clustering

## 2.1 Mahalanobis Distance Anomaly Detection

The Mahalanobis distance (M-dist) anomaly detector [6] assumes the background of the entire hyperspectral image can be well represented by a single Gaussian pdf. The likelihood function for the background is given by the following [6]

$$p_0(\mathbf{z}) = \frac{1}{\sqrt{(2\pi)^2 |\mathbf{C}_z|}} \exp\left\{-\frac{1}{2}(\mathbf{z} - \mathbf{m}_z)^T \mathbf{C}_z^{-1}(\mathbf{z} - \mathbf{m}_z)\right\}, \quad (5)$$

where  $\mathbf{m}_z$  is the global mean vector and  $\mathbf{C}_z$  is the global covariance matrix. In practice,  $\mathbf{m}_z$  and  $\mathbf{C}_z$  are sample estimates computed from background training data in which no target is present. If the targets are sufficiently small, the statistics can be estimated from the full scene

with some loss in performance due to target contamination. The decision statistic for the M-dist anomaly detector comes directly from (4) when (5) is used as  $p_0$ , and is given by

$$d_M(\mathbf{z}) = (\mathbf{z} - \mathbf{m}_z)^T \mathbf{C}_z^{-1} (\mathbf{z} - \mathbf{m}_z). \quad (6)$$

In (6), the pixels with the largest M-distance represent the most anomalous pixels. Figure 1 shows the decision statistic for a two band, simulated Gaussian distribution of image pixels. The pixels are represented by the blue dots and are assumed to have a mean vector  $\mathbf{m}_z$ , which is located at the center of the pixel distribution. The isocontour shown on the plot represents the decision statistic found in (6). Pixels near the mean in the blue regions of the isocontour are considered to be part of the Gaussian background model. Pixels located further from the mean in the red regions of the isocontour would be considered increasingly anomalous.

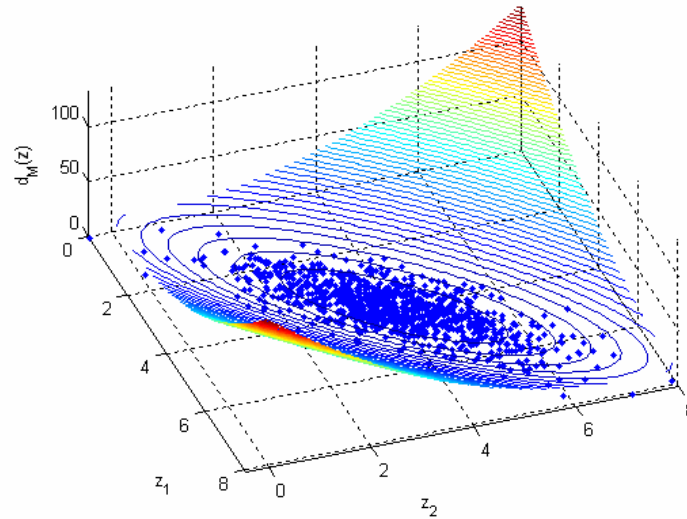


Fig. 1. Scatter plot for a single global Gaussian background model. The dots represent pixels in a simulated two band Gaussian distribution. The surface height is the global detection statistic for an observation at  $\mathbf{z}=[z_1, z_2]$ . The height is shown by the color coded isocontour. Pixels located close to the global mean (blue region) are classified as background pixels, while pixels falling far from the global mean (yellow, orange, red regions) are classified as anomalous.

## 2.2 Gaussian Mixture Model Anomaly Detection

The Gaussian mixture model (GMM) anomaly detector [6] is an extension of the M-dist anomaly detector. The GMM model uses a superposition of  $K$  Gaussians, each with its own mean and covariance, as the background likelihood function. In remote sensing applications, it is often appropriate to use such a model since the scene is likely to contain more than one type of background. The GMM background likelihood function is given by [6]

$$p_0(\mathbf{z}) = \sum_{k=1}^K P_z(k) \frac{1}{\sqrt{(2\pi)^2 |\mathbf{C}_z(k)|}} \exp\left\{-\frac{1}{2}(\mathbf{z} - \mathbf{m}_z(k))^T \mathbf{C}_z^{-1}(k)(\mathbf{z} - \mathbf{m}_z(k))\right\}, \quad (7)$$

where  $\mathbf{m}_z(k)$ ,  $\mathbf{C}_z(k)$ , and  $P_z(k)$  are the mean vector, covariance matrix and prior probability, respectively, of each of the  $k=1,2,\dots,K$  Gaussians. Here, these model parameters are estimated from the data using the stochastic expectation maximization algorithm (SEM) [9,10]. The decision statistic for the GMM anomaly detector is given by [6]

$$d_{GMM}(\mathbf{z}) = -\log \left\{ \sum_{k=1}^K P_z(k) \frac{1}{\sqrt{(2\pi)^2 |\mathbf{C}_z(k)|}} \exp \left\{ -\frac{1}{2} (\mathbf{z} - \mathbf{m}_z(k))^T \mathbf{C}_z^{-1}(k) (\mathbf{z} - \mathbf{m}_z(k)) \right\} \right\}. \quad (8)$$

This decision statistic is shown in Fig. 2 for a similar scenario as shown in Fig. 1, except that the background pixels are distributed among two Gaussian clusters. The method produces a smooth increasing decision statistic moving away from the center of the Gaussian clusters.

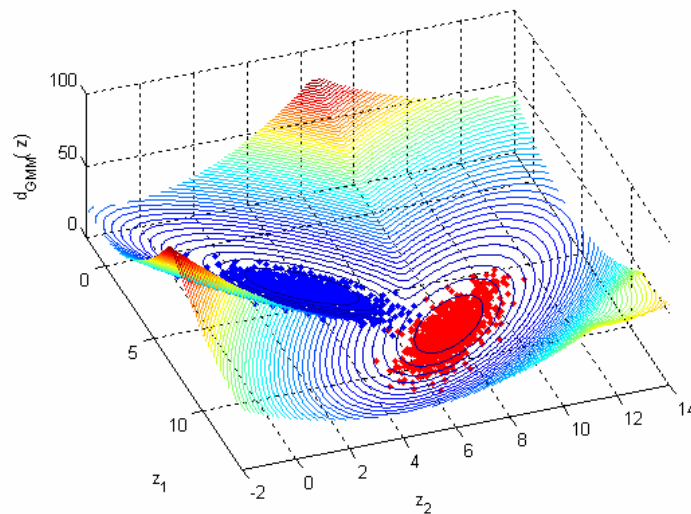


Fig. 2. Scatter plot for a two class GMM. The surface height is the GMM detection statistic for an observation at  $\mathbf{z}=[z_1, z_2]$ . Notice how the detection statistic rises as  $\mathbf{z}$  moves away from the clusters.

### 2.3 Reed-Xiaoli Anomaly Detection

The Reed-Xiaoli (RX) anomaly detector [12] is a locally adaptive method. The decision statistic is similar to the one given in (5), however  $\mathbf{m}_z$  and  $\mathbf{C}_z$  are estimated locally. These localized statistics are governed by two user controlled windows, the guard window and the background window. The guard window should be specified to be at least as big as the targets found in the scene. The size of the background window is somewhat subjective based on the scene in question, but should be larger than the guard window. A background window that is too small could cause problems in computing  $\mathbf{C}_z$ , while a window that is too large essentially eliminates the locally adaptive nature of the detector. Here the guard window is a square window of 81x81 pixels and the background window is a square window of 141x141 pixels. The statistics are computed from the pixels falling in between the guard and background windows. This area is shown in red in Fig. 3. The relatively large nature of the targets in the scene used in this study makes the RX detector very computationally demanding.

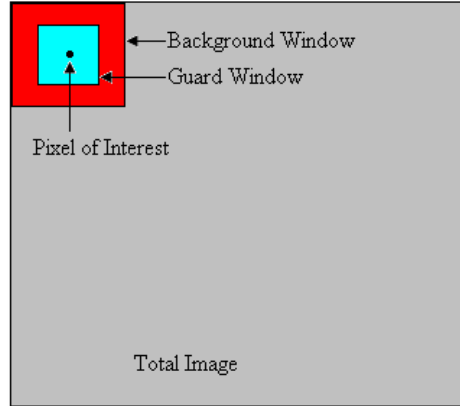


Fig. 3. Illustration of RX algorithm background statistic calculation.

## 2.4 Gaussian Mixture RX Anomaly Detection

The Gaussian mixture RX (GMRX) anomaly detector [6] also assumes that the background hyperpixels follow a Gaussian mixture model. The method requires the class *posteriori* probability, represented by [6]

$$P(k | \mathbf{z}) = \frac{p_0(\mathbf{z} | k)P_z(k)}{\sum_{k=1}^M p_0(\mathbf{z} | k)P_z(k)}. \quad (9)$$

The decision statistic for the GMRX detector is given by

$$d_{GMRX}(\mathbf{z}) = (\mathbf{z} - \mathbf{m}_z(q_{MAP}(\mathbf{z})))^T \mathbf{C}_z^{-1}(q_{MAP}(\mathbf{z}))(\mathbf{z} - \mathbf{m}_z(q_{MAP}(\mathbf{z}))), \quad (10)$$

where  $\mathbf{m}_z(q_{MAP}(\mathbf{z}))$  and  $\mathbf{C}_z(q_{MAP}(\mathbf{z}))$  are once again estimated for each Gaussian component using the SEM algorithm. The function  $q_{MAP}(\mathbf{z})$  is a maximum *a posteriori* (MAP) classifier of the form

$$q_{MAP}(\mathbf{z}) = \arg \max_k P(k | \mathbf{z}), \quad (11)$$

where  $P(k | \mathbf{z})$  is the posterior probability of class  $k$  given  $\mathbf{z}$ . The decision statistic for the GMRX detector is shown in Fig. 4. The thick blue line superimposed represents the MAP classifier decision boundary.

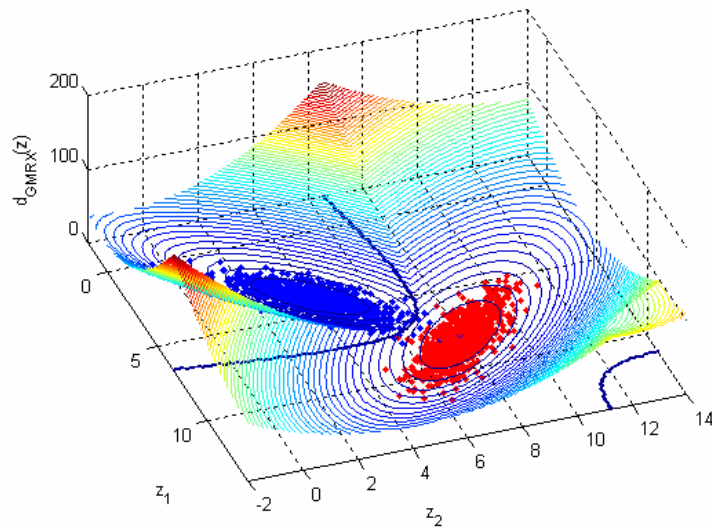


Fig. 4. Scatter plot for a two class GMRX. The surface height is the GMRX detection statistic for an observation at  $\mathbf{z}=[z_1, z_2]$ . The thick blue line represents the MAP classifier decision boundary. Notice the smooth decision statistics, similar to the GMM method.

## 2.5 Cluster-Based Anomaly Detection

The cluster-based anomaly detector (CBAD) [13] is very similar to the GMRX detector. The difference is that CBAD uses a k-means clustering algorithm [9] to estimate the component mean and covariance matrices and to segment the image. Unlike the previous methods, CBAD does not explicitly assume that the background model is Gaussian in nature. The decision statistic is a class based M-distance given by [13]

$$d_{CBAD}(\mathbf{z}) = (\mathbf{z} - \mathbf{m}_z(q_E(\mathbf{z})))^T \mathbf{C}_z^{-1}(q_E(\mathbf{z}))(\mathbf{z} - \mathbf{m}_z(q_E(\mathbf{z}))), \quad (12)$$

where  $\mathbf{m}_z(q_E(\mathbf{z}))$  represents a class mean and  $\mathbf{C}_z(q_E(\mathbf{z}))$  a class covariance. Instead of using a MAP classifier, CBAD determines a hyperpixel's class membership based on the minimum Euclidean distance measurement where

$$q_E(\mathbf{z}) : R^P \rightarrow \{1, 2, \dots, K\} \quad (13)$$

is the partition function given by

$$q_E(\mathbf{z}) = \arg \min_k \|\mathbf{z} - \mathbf{m}_k(\mathbf{z})\|^2. \quad (14)$$

Fig. 5 shows the decision statistic for a two class CBAD anomaly detector. Similar to previous methods discussed, the further a pixel is located from the nearest class the more anomalous it is. However, due to the Euclidean distance based clustering in (14), there is a very strong discontinuity in the decision statistic between the clusters. This is denoted by the very sharp edge between the two classes in Fig. 5.



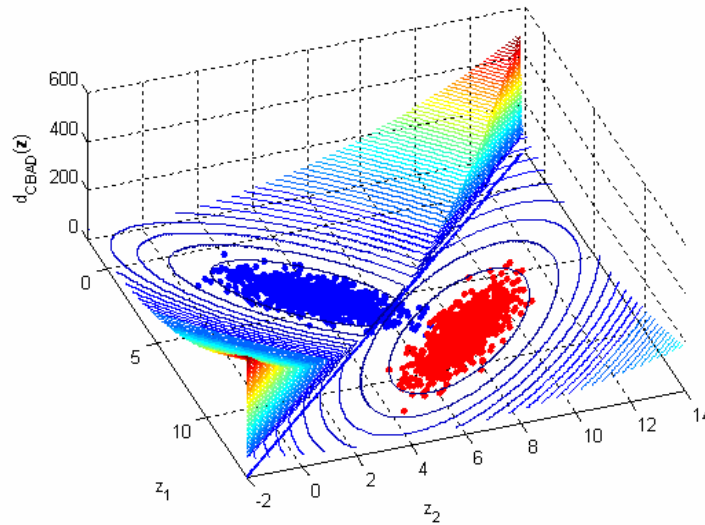


Fig. 5. Scatter plot for a two class CBAD. The surface height is the CBAD detection statistic for an observation at  $\mathbf{z}=[z_1, z_2]$ . Notice how the detection statistic has a discontinuity at the cluster boundary, denoted by the very sharp edge between clusters.

## 2.6 Fuzzy Cluster-Based Anomaly Detection

The fuzzy cluster-based anomaly detector (FCBAD) is a novel extension of the CBAD and GMRX algorithms in that it can include several possible membership functions. Like the CBAD method, FCBAD is not specifically linked to the assumption of a Gaussian background. The particular membership function used in this study is given as

$$q_k(\mathbf{z}) = \frac{1}{\left( (\mathbf{z} - \mathbf{m}_z(k))^T \mathbf{C}_z^{-1}(k) (\mathbf{z} - \mathbf{m}_z(k))^T \right)^P + 1}, \quad (15)$$

where  $P$  is a tuning parameter and  $\mathbf{m}_z(k)$  and  $\mathbf{C}_z(k)$  are class mean and class covariance, respectively. The tuning parameter,  $P$ , governs the sharpness between class transitions for the FCBAD algorithm [14]. Through analysis of experimental results it has been determined that the algorithm is not highly sensitive to this parameter. For the data used in this study,  $P=2$  was found to yield good results. Additionally, it should be noted that, among others, (11) or (14) can be substituted for (15), yielding the GMRX and CBAD detectors, respectively. The membership function is then used to compute the decision statistic

$$d_{FCBAD}(\mathbf{z}) = \sum_{k=1}^K q_k(\mathbf{z}) (\mathbf{z} - \mathbf{m}_z(k))^T \mathbf{C}_z^{-1}(k) (\mathbf{z} - \mathbf{m}_z(k)). \quad (16)$$

As with the CBAD detector, the model parameters of the FCBAD detector are estimates using k-means clustering [9]. Fuzzy clustering can also be applied to estimate model parameters, but doing so here did not yield improved performance. FCBAD does not have a hard decision statistic like the CBAD or GMRX detectors, giving it more flexibility. Additionally, this method may have performance benefits for non-Gaussian data in which the background has

heavy tails. Figure 6 shows the decision statistic for the two class FCBAD method. The blue lines represent the isocontours of the membership function given in (15) as it relates to the red cluster of pixels.

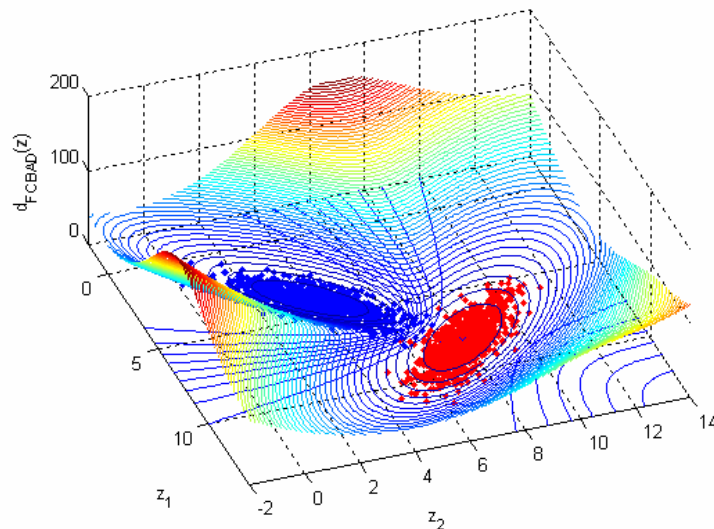


Fig. 6. Scatter plots for a two class FCBAD. The surface height is the FCBAD detection statistic for an observation at  $z=[z_1, z_2]$ . Note the smooth decision statistic isocontour and the membership function (blue lines) related to the red class of pixels.

### 3 CHANGE DETECTION

Change detection uses two images captured some time apart and seeks to identify relevant change between the two. The basic approach we apply is similar to that in Eismann, et al. [15] and it uses a predictor, temporal subtraction, and anomaly detection as shown in Fig. 7. The two data sets used in change detection analysis are referred to as the reference image (time 1),  $x$ , and the test image (time 2),  $y$ . If the two scenes are captured with some sizeable time interval apart, natural changes in the background of the scene will also be introduced. These natural changes may include illumination changes, shadowing and seasonal changes. It is desirable to eliminate or suppress these natural changes through a prediction process, which generates a transformation from the reference and test data sets. The transform is applied to create a predicted test image, which is then subtracted from the actual test image creating a residual error image. Ideally, the prediction and subtraction process removes the natural changes from the residual error image. The residual error image is then fed into an anomaly detector allowing for the extraction of relevant changes.

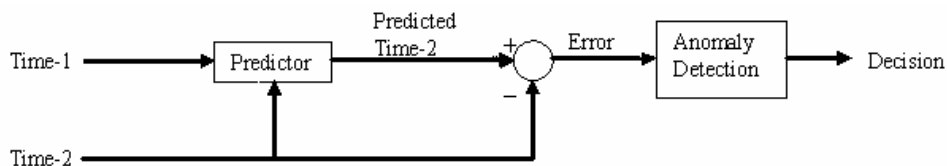


Fig. 7. Change Detection Process. The main components of interest are a predictor and an anomaly detector.

The Chronochrome (CC) algorithm [16] is one such change detector and it employs a linear predictor and an M-distance anomaly detector. Another approach to prediction is a segmented or cluster-based predictor. This method uses a clustering algorithm, such as k-means or SEM, to create a clustered prediction of the test data. This method is well covered in [15]. In our study here, we employ novel combinations of predictors and anomaly detectors and compare these to the CC and the other methods presented in [15]. In particular, we compare change detectors using selected detectors outlined in Section 2. We pair these anomaly detectors with linear and cluster-based predictors in hopes of identifying the most effective combination.

#### 4 HYPERSPECTRAL IMAGE ACQUISITION

The hyperspectral data sets referenced in this study are collected from August 2005 through May 2006, at Wright-Patterson Air Force Base, OH. These collections occur at specified times and solar positions to maintain continuity and provide a wide range of vegetation and illumination conditions. In all, over 100 data collections were performed and used in various studies; twelve diurnal collections and thirty six seasonal collections are used in this study. The single scene layout features a naturally vegetative environment with four painted aluminum panels set up to act as man-made anomalies. The scene layout is observed in Fig. 8. The panels are black, green, beige and silver in color, respectively. The test scene is deliberately artificial in nature in order to reduce the number of variables in the study. Due to its simplistic and artificial nature, the scene may not be typical of many remote sensing applications. However, the artificial nature allows for a more focused study of seasonal and diurnal environmental effects on anomaly and change detection algorithms.

The scene is captured by a Hyperspec VS-25 Imaging Spectrograph produced by Headwall Photonics that is placed 18 meters above the target level and across from the scene, as observed in Fig. 9. While the test scene is proximal in nature, it is believed that the results of the anomaly and change detection studies conducted also apply to non-proximal remote sensing applications. The imaging spectrometer is paired with a Dalsa Pantera TF 1M60 monochrome area scan CCD possessing a square focal plane containing an array of 1024 x 1024 pixels and a Navitar 50 mm lens. The system, which is mounted on a pan and tilt platform, possesses a spectral range in the visible to near infrared from 460 nm to 900 nm contained in 124 spectral bands.



Fig. 8. Color image of scene on May 8, 2006 at 1400 hrs.



Fig. 9. Overhead Panel and Camera Locations.

A spectral calibration is performed using a laser and gas lamps to determine the mapping coefficients. Additionally, a noise characterization of the system is performed to determine signal to noise levels for each pixel on the focal plane array [17]. An absolute radiometric calibration is performed to correct for the non-uniformity of pixel response. Finally, each data set is spectrally filtered to increase signal to noise ratio (SNR) using a low-pass filter.

After all the calibration procedures are complete, the data is reduced in dimensionality through a principal component transform in which the ten leading principal components are reserved for further analysis. The reason for using only the leading principal components is twofold. First, the hyperspectral data sets in their entirety are very large and are quite computationally intensive to process. Thus, reducing the size and computational intensity of the data was imperative to the success of a study such as this that analyzes a large number of data sets over diurnal and seasonal periods. Secondly, the vegetative background of the scene is well represented in this reduced principal component space [18]. Additionally, the targets in the test scene are relatively large in comparison to the overall scene. Their size ensures that they are represented in the reduced principal component space. Care is taken to ensure that the vast majority of the trailing principal component subspace is sensor noise [18]. However, due to the nature of the principal component transform some target features may reside in the trailing principal component space and are lost when it is discarded.

Figure 10 shows the spectra of the portion of the background containing trees and the green target for May 8 at 1400 hrs and Oct 18. The blue line represents the full 124 band spectra. The red line represents the spectra produced by the reverse principal component transform. In doing this comparison, the ten leading principal components are used and the trailing 114 principal component bands are replaced by the mean of each band. The covariance matrix used in the principal component transform is the same for each scene; the Aug 25 covariance matrix is used throughout. This was done as the data was originally intended for use in a several change detection studies. However, as shown in Fig. 10, the use of a single covariance matrix and only the leading principal components is deemed acceptable for this study as the losses are relatively minor. Additionally, the study only intends to reveal relative performance trends in anomaly and change detection. Future research into incorporating portions of the trailing subspace or the entire hyperspectral data product into anomaly and change detection algorithms, as well as using separate covariance matrices in the principal component transform could yield improved detection performance.

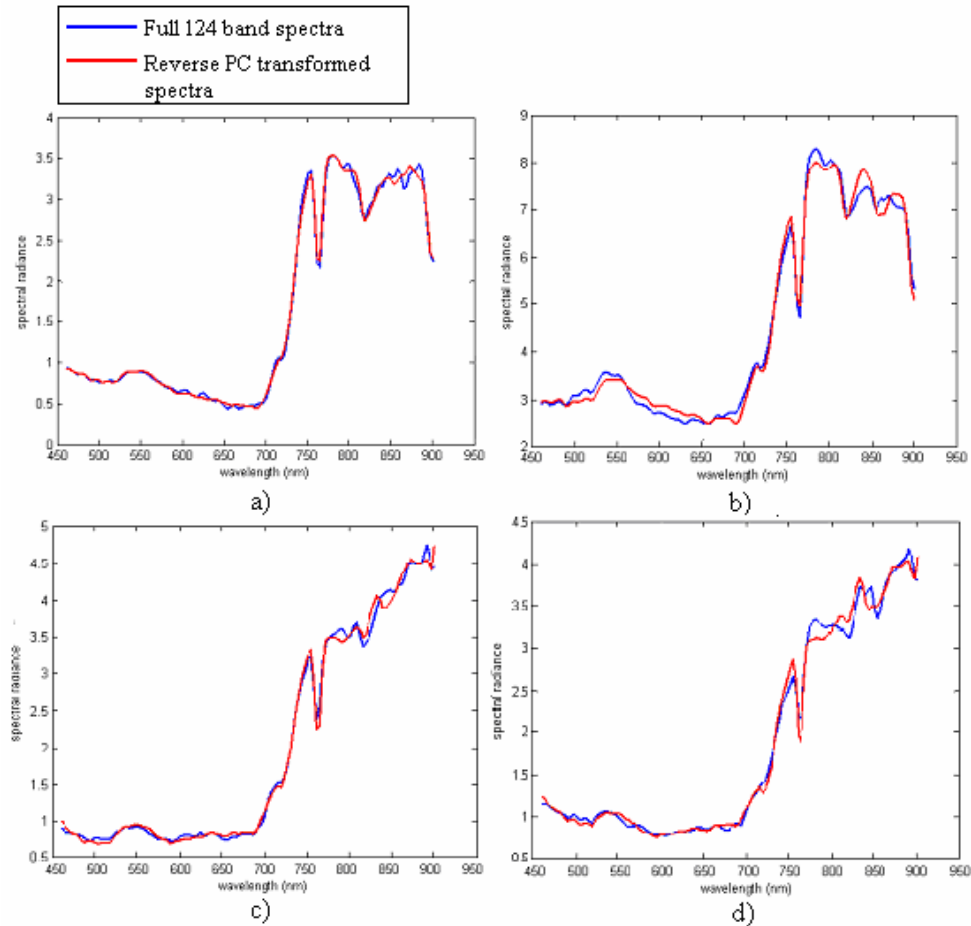


Fig 10. Spectral comparison between full and reduced dimensionality data: (a) May 8 trees (b) May 8 green target (c) Oct 18 trees, and (d) Oct 18 green target. The x-axis represents spectral radiance and the y-axis represents wavelength in nanometers. The blue line indicates the full 124 band spectra and the red line indicates the reverse transformed principal component spectra from the ten leading principal components.

## 5 EXPERIMENTAL RESULTS

### 5.1 Diurnal Data

Twelve hyperspectral data sets collected at Wright-Patterson Air Force Base over the period of 0800-1900 hrs (8 AM to 7 PM) on May 8, 2006 are selected for this diurnal data set. The overall diurnal data set allows for an examination of the effects of a wide range of solar positions and solar illuminations on the target scene. As a solar position reference, the solar azimuth is 81 degrees at 0800 hrs, 180 degrees at 1330 hrs and 278 degrees at 1900 hrs. Three separate experiments are used to evaluate the performance of each of the six anomaly detection methods. These experiments are explained in the next three sections and experimental results are presented in each. An example of the scene during the diurnal period at 1400 hours is shown in Fig. 8.

### 5.1.1 Performance vs. Time of Day

The first experiment measures and compares the area under the curve (AUC) calculated from the receiver operating characteristic (ROC) curves for each hyperspectral data set as a metric for detection performance [19,20]. The ROC curve is computed by counting correct detections and false alarms as the threshold level is increased from zero to the maximum detection statistic value. Example ROC curves can be seen in Figs. 15 and 19. As the detection threshold is raised in these figures, more pixels are classified as anomalies. Thus, a higher threshold leads to a higher probability that a true anomalous pixel will be detected and classified as an anomaly. However, as the threshold is raised the probability that non-anomalous pixels will mistakenly be classified as anomalies also goes up. Plotting the detection vs. false alarm results at each threshold creates a curve that characterizes the tradeoff between high detection probability and a high rate of false alarms. Figure 11 shows a portion of a ROC curve for three anomaly detection methods with three specific detection thresholds marked. This figure gives the user a general idea of the detection sensitivity of each method to the threshold level, and is useful for selecting an operating point for each anomaly detector. The AUC measures the area under the ROC curve to give a generalized anomaly detection performance evaluation. This is useful when large numbers of ROC curves become cumbersome to present.

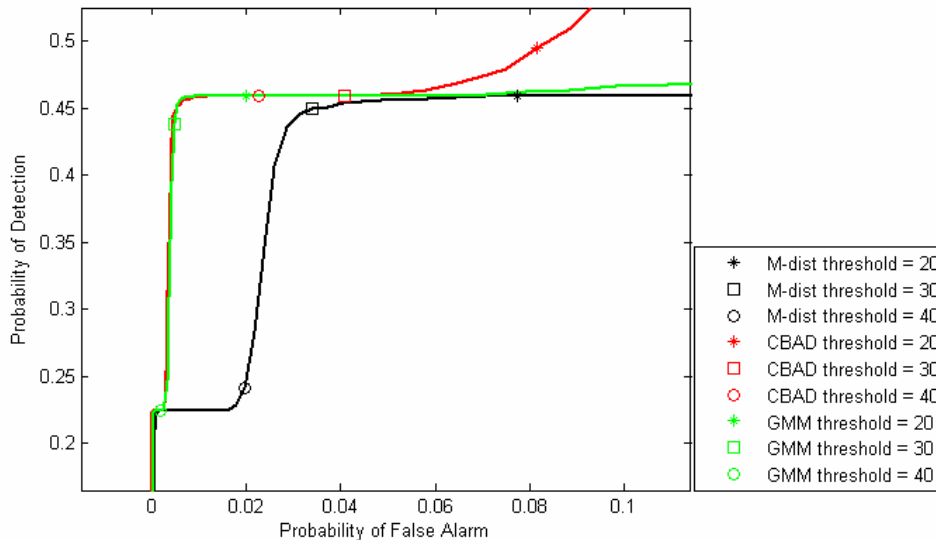


Fig. 11. ROC curve for Oct 18 with specific thresholds marked.

Figure 12 displays the anomaly detection images for each of the methods for May 8, 2006 at 1400 hours. The solar azimuth position at this time is 197 degrees. In these images brightness represents the decision statistic (i.e., bright pixels are more anomalous). All six methods are successfully able to detect and classify the four target panels as anomalies while raising few false alarms in the background. Figure 13 shows a portion of the ROC curves for each of the methods at 1400 hours. While CBAD has the best overall performance at this time, the overall difference between all six detection methods is minimal. Note the very small scaling on the x-axis of Fig. 13.

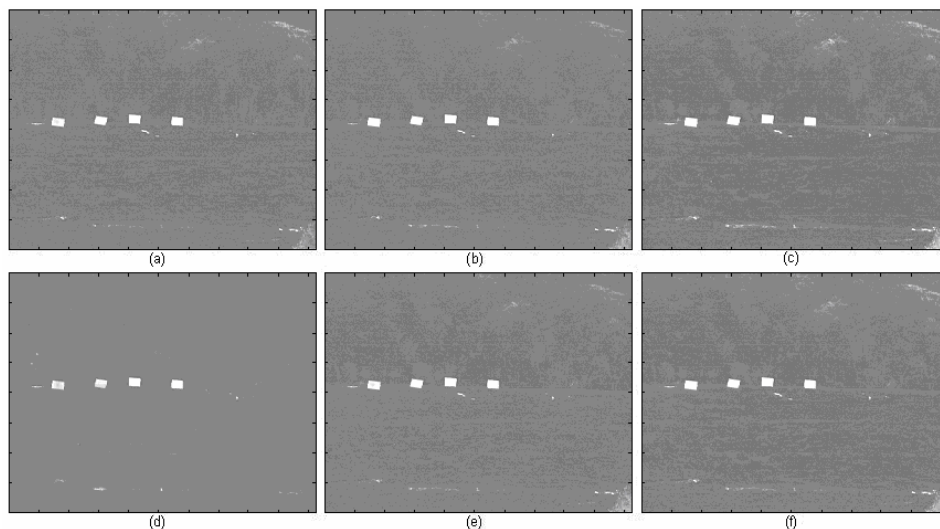


Fig. 12. Anomaly Detection Images May 8, 2006 at 1400 hrs – (a) M-distance, (b) CBAD, (c) GMM, (d) RX, (e) GMRX, (f) FCBAD.

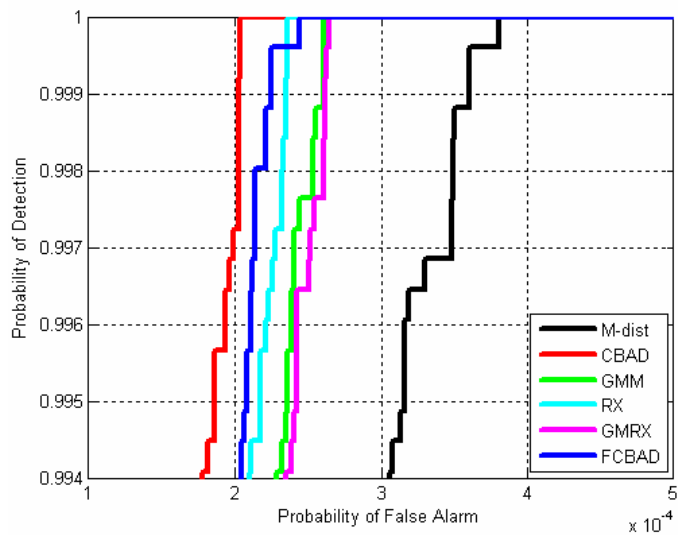


Fig. 13. ROC curves for May 8, 2006 at 1400 hrs. Note the very small probability of false alarms (x-axis) and the very high probability of detection (y-axis).

The AUC for all ROC curves during the diurnal period is now computed. Figure 14 shows the AUC of all six anomaly detection methods. Two classes are used where applicable. All detectors perform well from 0800-1700 hrs and have similar AUC values, as can be seen in Fig. 14.



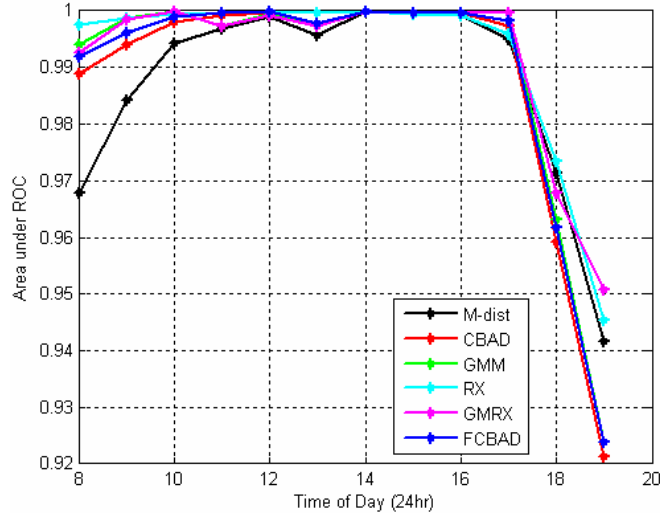


Fig. 14. Performance vs. Time of Day (0800-1900 hrs) with two classes used where applicable.

It is also noteworthy that all detectors have reduced performance between 1800-1900 hrs. This is due to illumination changes related to the solar angle with respect to the target panels. Between 1800-1900 hrs the sun slowly begins to set in the west, which is behind the northeast facing target panels. This causes a reduction in overall illumination on the panels and the scene in general, making anomaly detection more difficult. This illumination change is depicted in Fig. 15. An anomaly detection image at 1900 hrs is shown in Fig. 16 and a ROC curve for each method at 1900 hrs is provided in Fig. 17. Figure 16 clearly shows that the anomaly detectors have trouble detecting the two left most panels, black and green, respectively, at 1900 hrs. Note the much larger probability of false alarms (x-axis) in Fig. 17 as compared to the 1400 hrs case in Fig. 13.



Fig. 15. Color image of scene on May 8, 2006 at 1900 hrs.



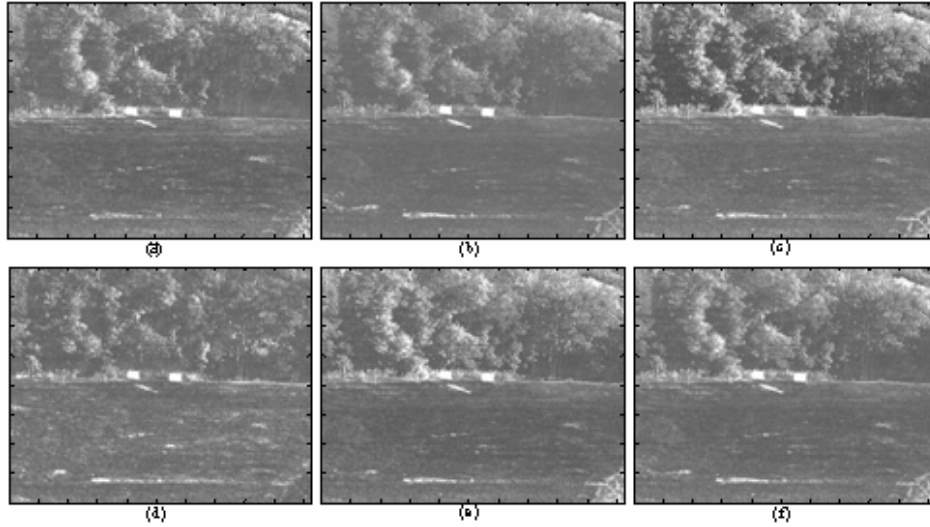


Fig. 16. Anomaly Detection Images May 8, 2006 at 1900 hrs – (a) M-distance, (b) CBAD, (c) GMM, (d) RX, (e) GMRX, (f) FCBAD.

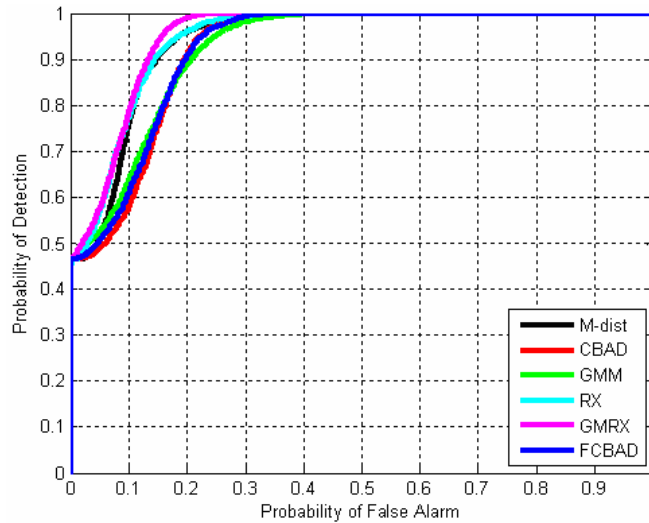


Fig. 17. ROC curves for May 8, 2006 at 1900 hrs.

Since the first principal component typically represents overall scene brightness, it is removed and the AUC is recomputed using principal components two through ten only. This experiment is shown to provide a 1-5% gain in detection performance for all methods during the 1800-1900 hr time period. However, removing the leading principal component was also found to modestly decrease the detection performance of all methods except the GMRX detector in the 0800-0900 hr time period.

### 5.1.2 Performance vs. Number of Classes

We now consider performance as a function of the number of classes used in the cluster-based methods (and superimposed  $K$  Gaussian methods GMM and GMRX, referenced as cluster-

based methods for simplicity from here on) varied between two and ten. The AUC values for the twelve diurnal data sets are averaged for each method and number of classes used. This provides a way to analyze the general performance tendencies among the six different anomaly detection methods as well as allowing an analysis of the effect of the number of classes in the cluster-based methods. No changes are made to the M-distance and RX detectors. Their performance is given for comparison and represented as flat lines. Results for all anomaly detection methods are shown in Fig. 18.

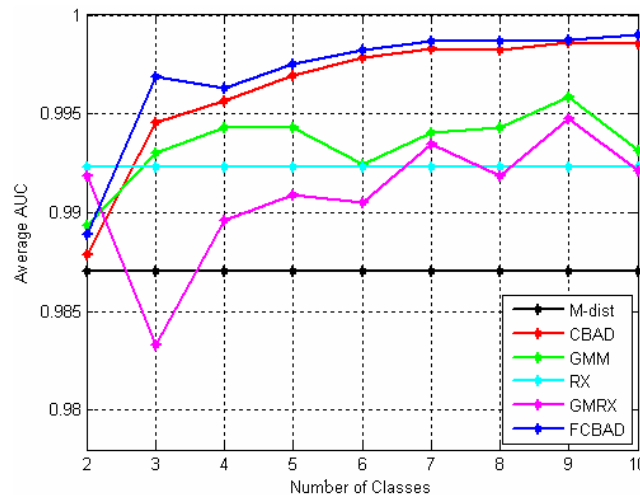


Fig. 18. Performance vs. Number of Classes.

Figure 18 shows that the addition of more classes generally increases the overall performance of the cluster-based methods. The FCBAD detector has the best performance, exhibiting a small advantage over the CBAD detector. Both increase steadily in performance with the addition of more classes, up until a point of diminishing returns around seven classes, likely due to the relative simplicity of the target scene used in the data collection process. A more complicated and populated scene would have a more diverse set of pixel values and therefore would likely support more classes. The GMM and GMRX methods also show some performance improvement with additional classes, but the gains are neither as large nor as consistent as with the CBAD and FCBAD methods. It is worth noting that the top performing methods, CBAD and FCBAD, use a relatively simple k-means clustering algorithm.

As was the case in section 5.1.1, the first principal component is once again removed to judge the detectors' overall sensitivity to scene brightness. Contrary to findings in section 5.1.1 for the two class case, the removal of principal component one is found to have less positive impact on detection performance as the number of classes increase. In fact, at four classes there is nearly zero performance gain in the 1800-1900 hr time period. At six classes and beyond the removal of the leading principal component moderately decreases detection performance for most methods over the same time period.

### 5.1.3 Performance with Target Contamination

In the previous two experiments, the statistics of the scene background are computed with the target panels completely masked out. This corresponds to a scenario where representative background training data are available and known to be free of targets. However, in many situations these types of training data are not available. In these situations it is sometimes necessary to use data where targets may be present, but relatively small compared to the

overall scene. In this experiment, the statistics of the background are degraded, or contaminated, by allowing a percentage of target panel pixels into the calculation. Target pixels are allowed to contaminate the scene at increments of ten percent. When 100% of the target pixels are included they account for roughly 0.3% of the total image pixels. This represents a more realistic, real world analysis of each detection algorithm's performance. Here, as in the second performance experiment, the AUC is averaged over all twelve data points. The results are shown in Fig. 19. The RX anomaly detector is not shown in this performance experiment since it does not use target masks and is not susceptible to target contamination.

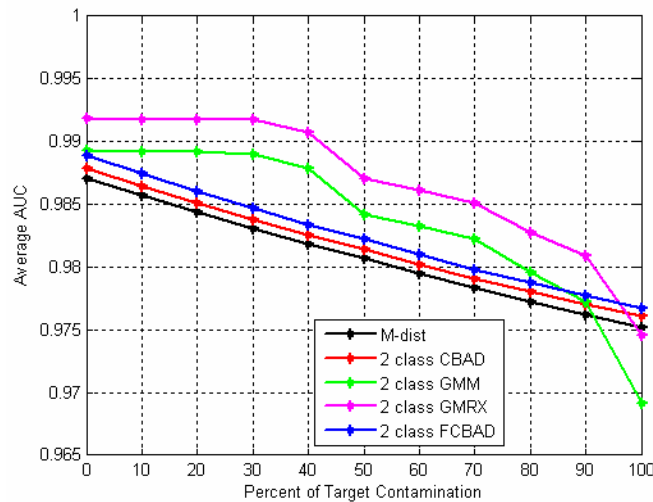


Fig. 19. Performance with Target Contamination with two classes used in the clustering methods.

Figure 19 shows the performance of the anomaly detection methods with respect to the percentage of target contamination present. All of the clustering methods are shown for the simple two class case. As seen in Fig. 19, the performance of all the methods is degraded as more target pixels are included. The performance of the M-distance, CBAD and FCBAD detectors fall at a fairly constant, linear rate throughout. The GMM and GMRX detectors exhibit less uniform behavior and some resistance to small amounts of target contamination; however, they are generally negatively affected by target contamination as well.

## 5.2 Seasonal Data

The seasonal data set consists of thirty six hyperspectral data sets collected at Wright-Patterson Air Force Base between August 24, 2005 and April 18, 2006. These data collections represent a wide range of seasonal conditions, including full illumination, distinct shadowing and light snow cover. All sets have a constant solar position in which the solar azimuth is fixed at 180 degrees. The same three performance experiments used to analyze the diurnal data are also applied to the seasonal data.

### 5.2.1 Performance vs. Season

The AUC is computed for the thirty six seasonal data sets. The results are shown in Fig. 20 and two classes are used in the clustering methods throughout section 5.2.1.

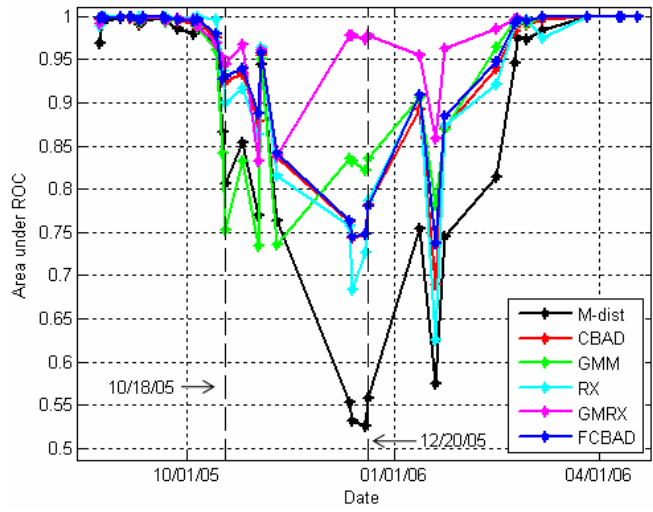


Fig. 20. Performance vs. Season with two classes used where applicable.

Clearly visible in Fig. 20 are three distinct regions of performance. Two regions in which all the detection methods exhibit excellent performance are seen from the beginning of the collection (August 24, 2005) through mid-October 2005 and from March 2006 through the end of the collection on April 18, 2006. Scene illumination and environmental conditions during these periods is comparable to the conditions shown in Fig 8. Anomaly detection performance during these periods is similar to the performance shown in Figs. 12 and 13. In the third region between mid-October 2005 and early March 2006, the performance of all detectors is highly degraded. This results from distinct shadowing features that enter the scene and engulf all four target panels. In addition, the scene background in the December collection data is covered in a light layer of snow (the target panels are not covered). Examples of the shadowing effects and snow cover are shown as color images in Figs. 21 and 22. These figures represent October 18, 2005 at 1330 hrs and December 20, 2005 at 1230 hrs, respectively. October 18 and December 20 date lines are also marked in Fig. 20 to more easily identify AUC performance. The anomaly detection images are shown in Figs. 23 and 24 and the ROC curves of all six methods can be seen in Figs. 25 and 26.



Fig. 21. Color image of scene on Oct 18, 2005.



Fig. 22. Color image of scene on Dec 20, 2005.

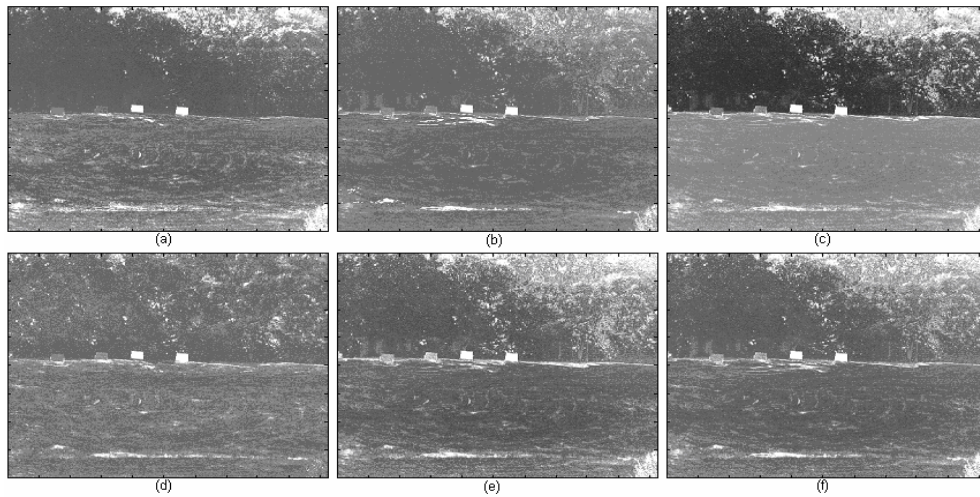


Fig. 23. Anomaly Detection Images for October 18, 2005 – (a) M-distance, (b) CBAD, (c) GMM, (d) RX, (e) GMRX, (f) FCBAD.

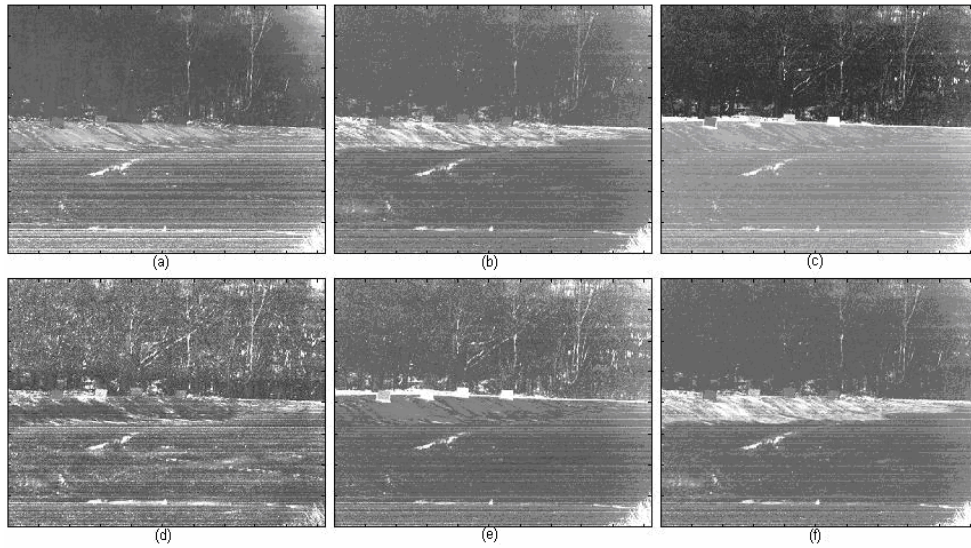


Fig. 24. Anomaly Detection Images December 20, 2005 – (a) M-distance, (b) CBAD, (c) GMM, (d) RX, (e) GMRX, (f) FCBAD.

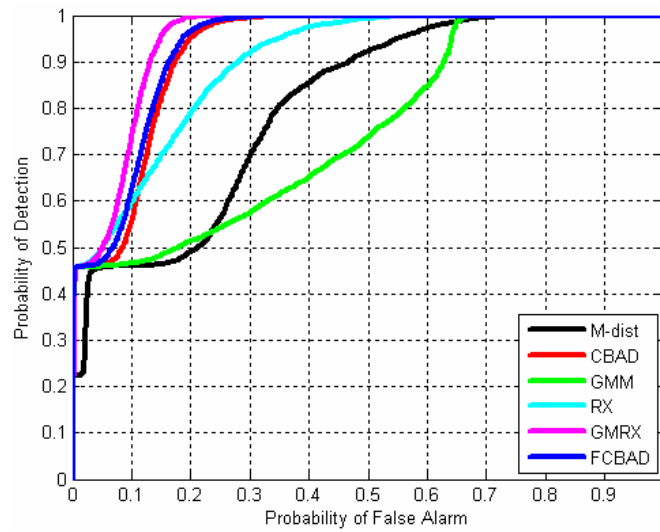


Fig. 25. ROC curves for Oct 18, 2005.



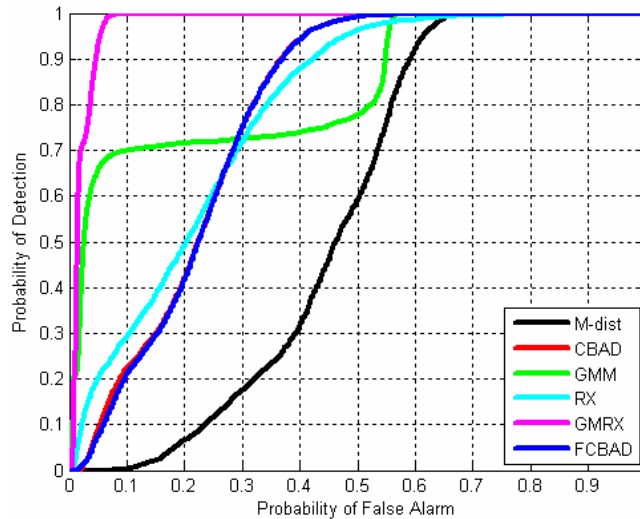


Fig. 26. ROC curves for Dec 20, 2005.

As can be seen in Figs. 23-26, the detection performance of all six methods is negatively impacted by the shadowing effects and snow cover in the scene. During the shadowed period, Fig. 23 shows that the two left most targets, black and green respectively are the most difficult for the detectors to properly classify as anomalies. There are also a very significant number of false alarms raised in the background. This decreased performance is also seen in the ROC curve in Fig. 25. As is shown in Figs. 24 and 26, the performance of the methods degrades further in the presence of snow cover. In general, the methods fail to classify the target panels as anomalous. The exceptions here are the GMM and GMRX methods. The GMM method shows some ability to successfully operate under adverse conditions and is able to detect three target panels as seen in Fig. 24 (c). The GMRX method exhibits good detection performance despite the shadowing and snow cover. Figure 24 (e) shows that the GMRX method is able to classify all four target panels as anomalies, despite the adverse conditions. This performance advantage is also seen in the ROC curve in Fig. 26. It is worth noting that both the GMM and GMRX methods use stochastic expectation maximization as their clustering algorithms.

The anomaly detection performance degradation is due to illumination changes in the scene. Figure 27 illustrates the fundamental changes in the scene during periods of shadowing and snow cover in the form of a scatter plot of principal component 1 vs. principal component 2. Figure 27 (a) represents May 8, 2006 at 1400 hrs, which is a well illuminated data set with a solar azimuth position near 180 degrees. Figure 27 (b) represents December 20, 2005, a data set in which shadowing and a light layer of snow are present. In the figure, the lower portion of the background consisting of grass is represented by red diamonds and the upper portion consisting of trees is represented by blue diamonds. The black, green, beige and silver targets are represented by cyan, green, magenta and yellow X's, respectively. It is clear from Fig. 27 (a) that under near optimum illumination conditions, the targets generally separate from the background, allowing them to be easily detected as anomalies by all detectors. In Fig. 27 (b), however, the target pixels tend to intermix with the background pixels. This intermixing makes it especially difficult for linear and locally adaptive methods to detect the man-made panels as anomalous from the background. The cluster-based anomaly detectors are able to more accurately model the background represented in Fig. 27 (b), and thus have more success identifying anomalies.

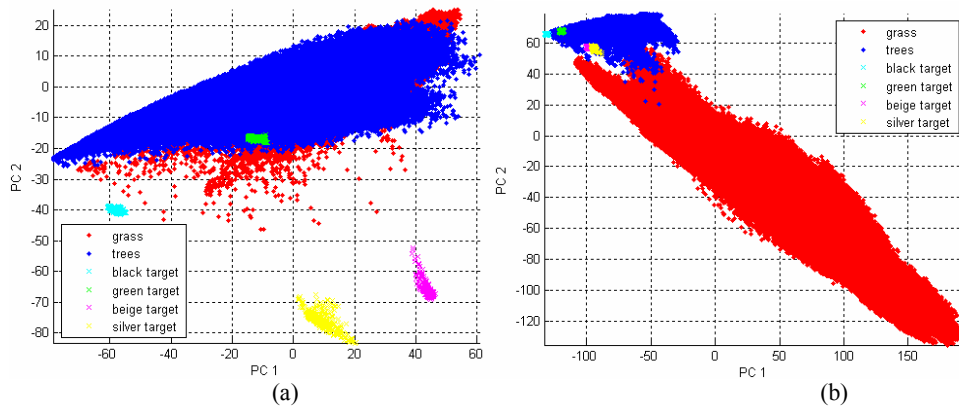


Fig. 27. Scatter plots of PC 1 vs. PC 2 – (a) May 8, 2006, (b) Dec 20, 2005.

Figure 28 illustrates the target-to-background separability of anomaly detection methods. In this case the CBAD method is shown in conjunction with data from May 8 at 1400 hrs. The decision statistic assigned to a pixel by the CBAD method is shown along the x-axis, while the number of pixels assigned to that particular decision statistic is shown on the y-axis. Figure 28 clearly shows that the majority of the background pixels are assigned decision statistics near or below 100. Targets are generally assigned higher decision statistics.

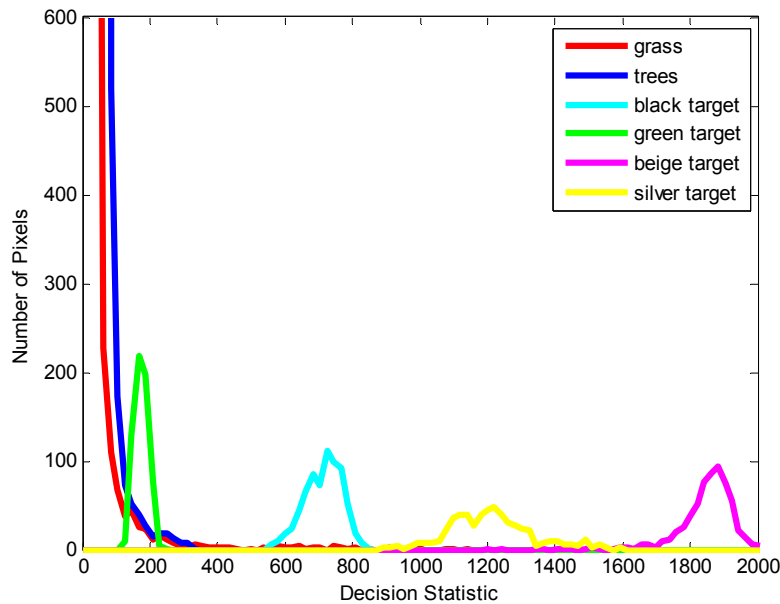


Fig. 28. Target-to-background separability. Data from May 8 @ 1400 hrs using the CBAD method with 4 classes.

To remain consistent with the experimentation in section 5.1.1, the first principal component is now removed and the AUC is recomputed for the seasonal period using the remaining principal components. Generally, this removal is found to decrease the performance of all anomaly detectors over the seasonal period.



### 5.2.2 Performance vs. Number of Classes

A similar performance experiment is used in this section as in the earlier section analyzing performance as a function of the number of clustering classes used. In that previous section, the general behavior of the detection methods as a function of the number of classes used is discovered for highly illuminated, non-shadowed data sets. Instead of repeating that analysis in this section, only the data points that feature a highly shadowed scene are used. This allows a more thorough breakdown of the ability of the six methods to classify anomalies in the presence of the adverse conditions of shadowing and snow cover. The results are shown in Fig. 29.

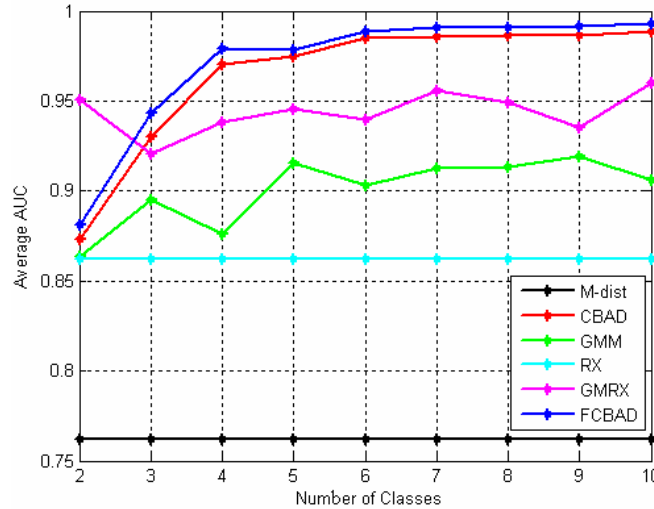


Fig. 29. Performance vs. Number of Classes using only the seventeen shadowed data sets from mid October 2005 – early March 2006.

As seen in Fig. 29, with the exception of the GMRX method which has near peak performance in the two class case, the overall performance of the cluster-based methods increases with the addition of more clustering classes up until a point of diminishing returns. This is similar to the behavior observed for the diurnal data sets in Fig. 18. In Fig. 29, however, the difference between the minimum and maximum achieved performance is much greater. As before, the performance of the CBAD and FCBAD detectors is closely related. These methods have the best overall performance during the shadowed seasonal period, with a diminishing returns behavior beginning at six clustering classes. The GMM detector's performance also benefits from the addition of classes, although the performance gains are not as strong as with CBAD and FCBAD. The GMRX method also exhibits similar behavior to that seen in Fig. 18. The GMRX method features very good performance with only two classes, but does not benefit appreciably from the addition of more classes. In the shadowed seasonal period, the cluster-based methods significantly outperform the global and locally adaptive anomaly detection methods.

Once again, the first principal component is removed and the AUC is recomputed for the seasonal data with a varying number of classes. The removal is found to seriously decrease the detection performance of all methods over the seasonal period.

### 5.2.3 Performance with Target Contamination

The performance experiment used in this section is similar to the third performance experiment used in the diurnal case. Here, similar to the previous section, only the shadowed data sets are used. The results are shown in Fig. 30.

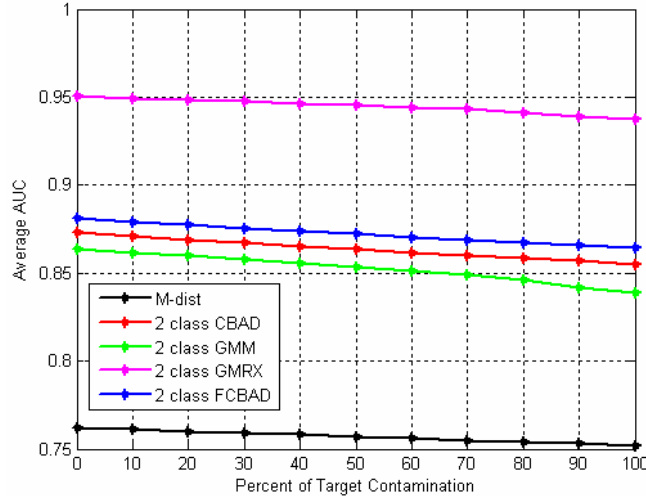


Fig. 30. Performance with Target Contamination using only the seventeen shadowed data sets from mid October 2005 – early March 2006.

The performance in Fig. 30 is as expected, with all detectors having reduced performance as target pixel contamination increases. Unlike the somewhat varying nature seen for the GMM and GMRX detectors in the diurnal data in Fig. 19, the relationship between performance and target contamination is fairly linear for all detectors.

### 5.3 Change Detection

The experimentation conducted on change detection follows closely with the work of Eismann, et al. [15]. In that work, the idea of a segmented (cluster-based) prediction algorithm paired with an M-dist or RX anomaly detector is investigated. The cluster-based predictor can employ either the k-means or SEM clustering methods. In this study, that prediction-anomaly detection combination is compared to a change detection combination where the CC and cluster-based predictors are paired with cluster-based anomaly detectors. Six classes are used in cluster-based prediction and anomaly detection throughout this experiment. The prediction-anomaly detection combinations are outlined in Table 2.

Table 2: Change Detection Combinations

Predictor	Anomaly Detector
CC (global)	CBAD
CC (global)	GMRX
Segmented (K-means)	M-dist
Segmented (SEM)	M-dist
Segmented (K-means)	CBAD
Segmented (SEM)	GMRX

The reference and test images are chosen to be October 26, 2005 and October 14, 2005, respectively. It should be pointed out that these are in reverse chronological order, as only a limited number of appropriate test images are available. October 14 happens to fall just inside the time period where shadowing becomes a serious issue in the scene, as described in previous sections. With the test image selected, it is then desired to choose an appropriately shadowed reference image that is collected a reasonable period of time from the test image. October 26 is judged to be a reasonable selection despite the reverse chronological order. The reference and test images are shown in Figs. 31 and 32.



Fig. 31. Reference Image Oct 26, 2005.



Fig. 32. Test Image Oct 14, 2005.

Differing from previous experimentation, the four aluminum target panels are considered part of the background and are not desired to be detected as anomalies. Instead, two bundled green tarps (circled) are added to the test scene as shown in Fig. 32. These are the targets we desire to identify through the change detection process while suppressing the natural changes from scene to scene. The change detection performance of each predictor-anomaly detector combination is shown in Fig. 33. Background statistics for the scene are computed from the reference image and applied throughout the process, where applicable. No target masks are used in the statistical calculations or in the prediction process.

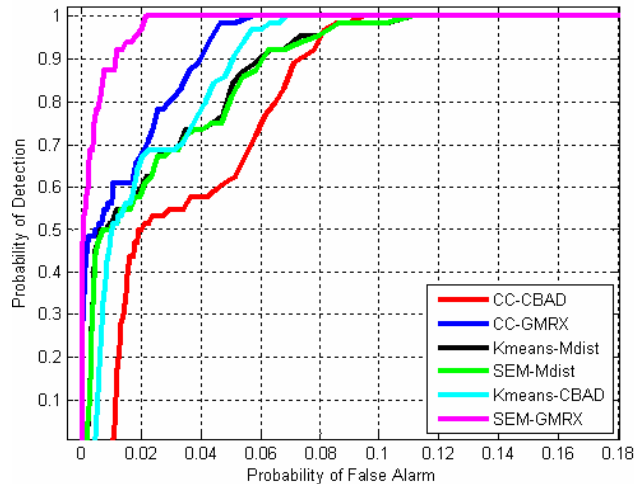


Fig. 33. ROC curve for Change Detection Combinations.

Figure 33 shows all predictor-detector combinations have relatively strong change detection performance. The combination of SEM prediction and GMRX anomaly detection has the best overall performance. This performance, coupled with the strong performance of the CC predictor and GMRX anomaly detector combination suggest the use of GMRX anomaly detection with statistics computed from the reference image is preferred for change detection.

## 6 CONCLUSIONS

For the diurnal data study, all six anomaly detection methods have very high detection performance. The overall difference between the best and worst performing detectors is small. All methods exhibit a degradation of detection performance in the late afternoon and early evening caused by the reduction of overall scene illumination due to the solar angle of the setting sun.

For the seasonal data study, scenes in which the target panels are highly illuminated with no shadowing effects led to detector performance similar to that of the diurnal data sets. Under conditions with significant shadowing and snow cover, the performance of the detection methods is distinctly different. Here, the cluster-based methods exhibit significantly improved performance compared to the global and locally adaptive methods. In general, the performance of the cluster-based methods benefits from the addition of clustering classes up to about six. The additional clusters provide a level of robustness to the detectors, allowing them to operate with improved performance in adverse conditions. The exception is the GMRX detector, which displays nearly its best performance with only two clustering classes. FCBAD with six clustering classes features the best overall performance during shadowed conditions, holding a slight advantage over the CBAD detector.

Most anomaly detection performance degradation stems from distinct shadowing or illumination changes in the scene. Generally, the leading principal component is associated with overall scene brightness. To measure the effect of scene brightness on anomaly detection performance the leading principal component is removed and the experiments conducted in sections 5.1.1, 5.1.2, 5.2.1 and 5.2.2 are repeated using the remaining nine principal components. This removal is found to aid the anomaly detection performance of all methods in the diurnal two-class case for the 1800-1900 hr time interval. In all other cases, removing the leading principal component does not aid performance.

As expected, target pixel contamination has a negative effect on the performance of all detection methods. During the diurnal study, the GMM and GMRX detectors show some resistance to this negative performance affect. This resistance is not present in the seasonal study where the detection performance varies almost linearly with the fractional target contamination. The detectors experience a 1-3% percent reduction in the area under the Receiver Operating Characteristic curve when all of the target pixels are allowed to contaminate the background statistics.

In the change detection study, the segmented SEM based predictor coupled with a GMRX anomaly detector yields the best overall change detection performance. Additionally, the second best performing combination is a CC predictor coupled with a GMRX anomaly detector. These results support the use of a GMRX anomaly detector to achieve optimum results during the change detection process.

## References

- [1] A. Goetz., G. Vane, J. Solomon, and B. Rock, "Imaging spectrometry for earth remote sensing," *Science* **228**, 1147-1153 (1985) [doi:10.1126/science.228.4704.1147].
- [2] L. Kumar, K. S. Schmidt, S. Dury, and A. K. Skidmore, "Imaging spectrometry and vegetation science," *Imaging Spectrometry: Basic Principles and Prospective Applications*, F.D. van der Meer and S.M. DeJong (Eds.), pp. 306-359, Springer, Dordrecht, The Netherlands (2002).
- [3] B. Stevenson, R. O'Connor, W. Kendall, A. Stocker, W. Schaff, D. Alexa, J. Salvador, M. Eismann, K. Barnard, and J. Kershenshtein, "Design and performance of the Civil Air Patrol ARCHER hyperspectral processing system," *Proc. SPIE* **5806**, 731-742 (2005) [doi:10.1117/12.604471].
- [4] A. Zare, J. Bolton, P. Gader, and M. Schatten, "Vegetation mapping for landmine detection using long-wave hyperspectral imagery," *IEEE Trans. Geosci. Rem. Sens.* **46**, 172-178 (2008) [doi:10.1109/TGRS.2007.906438].
- [5] D. Manolakis and G. Shaw, "Detection algorithms for hyperspectral imaging applications," *IEEE Signal Process. Mag.* **19**(1), 29-43 (2002) [doi:10.1109/79.974724].
- [6] D. W. Stein, S. G. Beaven, L. E. Hoff, E. M. Winter, A. P. Schaum, and A. D. Stocker, "Anomaly detection from hyperspectral imagery," *IEEE Signal Process. Mag.* **19**(1), 58-69 (2002) [doi: 10.1109/79.974730].
- [7] M. J. Carlotto, "Detection and analysis of change in remotely sensed imagery with application to wide area surveillance," *IEEE Trans. Image Process.* **6**(1), 189-202 [doi:10.1109/83.552106].
- [8] A. Schaum and A. Stocker, "Subclutter target detection using sequences of thermal infrared multispectral imagery," *Proc. SPIE* **3071**, 12-22 (1997) [doi:10.1117/12.280605].
- [9] J. A. Hartigan and M. A. Wong, "A K-means clustering algorithm," *J Roy. Stat. Soc. C Appl. Stat.* **28**(1), 100-108 (1979) [doi:10.2307/2346830].
- [10] M. T. Eismann and R. C. Hardie, "Initialization and convergence of the stochastic mixing model," *Proc. SPIE* **5159**, 307-318 (2004) [doi:10.1117/12.499680].
- [11] M. T. Eismann and R. C. Hardie, "Application of the stochastic mixing model to hyperspectral resolution enhancement," *IEEE Trans. Geosci. Rem. Sens.* **42**, 1924-1933 (2004) [doi:10.1109/TGRS.2004.830644].
- [12] L. S. Reed and X. Yu, "Adaptive multiple-band CFAR detection of an optical pattern with unknown spectral distribution," *IEEE Trans. Acoust. Speech Signal Process.* **38**, 1760-1770 (1990) [doi:10.1109/29.60107].

- [13] M. J. Carlotto, "A cluster based approach for detecting man-made objects and changes in imagery," *IEEE Trans. Geosci. Rem. Sens.* **43**(2), 374-387 (2005) [doi:10.1109/TGRS.2004.841481].
- [14] M. Shao and K. Barner, "Optimization of partition-based weighted sum filters and their application to image denoising," *IEEE Trans. Image Process.* **15**(7), 1900-1915 (2006) [doi:10.1109/TIP.2006.873436].
- [15] M. T. Eismann, J. Meola and R. C. Hardie, "Hyperspectral change detection in the presence of diurnal and seasonal variations," *IEEE Trans. Geosci. Rem. Sens.* **46**, 237-249 (2008) [doi:10.1109/TGRS.2007.907973].
- [16] A. Schaum and A. Stocker, "Advanced algorithms for autonomous hyperspectral change detection," *33rd Applied Imagery Pattern Recognition Workshop*, pp 33-38 (2004) [doi:10.1109/AIPR.2004.10].
- [17] R. Radke, S. Andra, O. Al-Kofahi, and B. Roysam, "Image change detection algorithms: a systematic survey," *IEEE Trans. Image Process.* **14**(3), 294-307 (2005) [doi:10.1109/TIP.2004.838698].
- [18] J. Meola, "Analysis of hyperspectral change and target detection as affected by vegetation and illumination variations," PhD Thesis, University of Dayton (2006).
- [19] J. P. Egan, *Signal Detection Theory and ROC-analysis*, Academic Press, New York (1975).
- [20] R. A. Maxion and R. R. Roberts, "Proper use of ROC curves in Intrusion/Anomaly Detection," **Technical Report Series CS-TR-871**, School of Computing Science, University of Newcastle (2004).

**Patrick C. Hytla** received the B.S. and M.S. degrees in electrical engineering from the University of Dayton, Dayton, OH in 2005 and 2007, respectively. He is currently an Image Processing Engineer with the University of Dayton Research Institute (UDRI) in Dayton, OH. Prior to joining UDRI, he worked as a Research Assistant with the University of Dayton's Electrical and Computer Engineering Department. His current research involves resolution enhancement and scene-based non-uniformity correction for remote sensing applications. Other research interests include target detection and classification in hyperspectral imagery.

**Russell C. Hardie** received the B.S. degree in engineering science from Loyola College, Baltimore, MD, in 1988 and the M.S. and Ph.D. degrees in electrical engineering from the University of Delaware, Newark, in 1990 and 1992, respectively. He is currently a Full Professor with the Department of Electrical and Computer Engineering, University of Dayton, Dayton, OH and holds a joint appointment with the Electro-Optics Program. Prior to joining the University of Dayton, he was a Senior Scientist with the Earth Satellite Corporation, MA. His research interests include a wide variety of topics in the area of digital signal and image processing such as image enhancement and restoration, pattern recognition, and medical image processing.

**Michael T. Eismann** is the Electro-Optical Sensor Technology Division technical advisor at the Sensors Directorate of the Air Force Research Laboratory (AFRL), Wright-Patterson Air Force Base, Ohio. He is responsible for overseeing the development of electro-optical and infrared sensor technology, and transition into operational airborne targeting and reconnaissance systems. Prior to joining AFRL, he was employed by the Environmental Research Institute of Michigan (ERIM), where he was involved in research concerning active and passive optical and infrared targeting and reconnaissance, optical information processing, and holographic optics. He has a B. S. in Physics from Thomas More College, an M. S. in Electrical Engineering from the Georgia Institute of Technology, and a Ph. D. in Electro-Optics at the University of Dayton.

**Joseph Meola** received the B.S. and M.S. degrees in electrical engineering from the University of Dayton, Dayton, OH in 2004 and 2006, respectively. He is currently a Research Engineer with the Electro-Optical Targeting Branch, Sensor Directorate of the Air Force Research Laboratory (AFRL), Wright-Patterson Air Force Base, OH. Prior to joining AFRL, he worked as a Research Assistant with the University of Dayton while obtaining the M.S. degree in electrical engineering. His current research involves image processing, target-detection algorithms, and the development and characterization of hyperspectral imaging sensors. In particular, his current efforts involve change detection work using hyperspectral imagery.